Fatigue process of rib-to-deck welded joints of orthotropic steel decks

Benjin Wang[a], Wim Nagy[b], Hans De Backer[b], Airong Chen[c],*

[a] School of Aerospace Engineering and Applied Mechanics, Tongji University, Shanghai 200092, China
[b] Department of Civil Engineering, Ghent University, Zwijnaarde 9052, Belgium
[c] Department of Bridge Engineering, Tongji University, Shanghai 200092, China

ABSTRACT

The numerous welded joints in orthotropic steel decks (OSDs) lead to a high probability of fatigue damage. One of the most detrimental problems is the severe reduction of the serviceability due to cracks in rib-to-deck welded joints, which require in-depth studies on the entire fatigue process. The linear elastic fracture mechanics has been proven to be effective in this aspect. When put into practice on actual projects, however, its accuracy and feasibility are largely dependent on features in various scales. This paper presents an investigation on the fatigue behavior of orthotropic steel decks with respect to multiscale concerns. By performing fatigue tests on OSD specimens welded by 15-mm-thick deck plates and 6-mm-thick stiffeners of S355 steel, the rib-to-deck weld toe crack that penetrates the deck plate is produced and the crack growth path is addressed using beach mark method. Afterwards, a two-dimensional local model of the rib-to-deck weld toe crack is built using the extended finite element method by which the stress intensity factors for early-stage cracks can be obtained. Based on the similar concept of nominal stresses, it can easily be linked to the macroscopic model and forms a non-concurrent method that enables to simulate the crack growth at rib-to-deck weld toe. As a result, a crack growth rate curve for the test specimen is given and different stages are analyzed with respect to the Paris law, indicating a clear influence of the early-stage fatigue cracks. The material constants of crack growth are obtained and validated, which may further be introduced to the fatigue assessment and life estimation for the maintenance work of OSDs.

1. Introduction

As a common structural type in steel bridge design, the orthotropic steel deck (OSD) is favored for its mechanical efficiency in terms of load carrying capacity per unit weight. However, the fatigue performance remains a key issue, as OSD is one of the most-reported structures suffering from fatigue problems. According to previous reports on actual bridges [1–3], the most fatigue-prone details of OSDs are the welded joints and adjacent areas. Studies on this issue were therefore mainly focused on the local effects for the fatigue performance of various details on OSDs, including the rib-to-deck welded joint [4,5], the butt welded joint of the ribs [6], the rib-to-diaphragm welded joint and the cutout [7], etc.

The fatigue cracks on the rib-to-diaphragm welded joints and the cutouts are in fact the most common types among all [8], though the caused damage is not so critical in terms of safety and serviceability. In contrast, the fatigue assessment for the rib-to-deck welded joint, even though fewer fatigue cracks are found, is of greater importance. The reason is partly because of the difficulty in detecting and identifying a crack in the rib-to-deck welded joint, especially for that starts from the weld root. More importantly, it could largely reduce the local stiffness of OSD, and directly lead to the failure of pavements, which will be quite devastating to the serviceability of the bridge. As a consequence, even though the OSD structure still keeps a certain level of robustness itself, it will be considered as severely damaged and have to be retrofitted, or in the worst case, re-built.

Hence, the definition of fatigue failure for OSDs should give more credit to the fatigue process, rather than just focusing on the fatigue failure life obtained by testing. It means the classical stress-life relation is not applicable due to its omission of the crack growth process. With respect to that, the introduction of fracture mechanics will provide a way to further investigate the fatigue problem of OSDs. For this kind of large-scale engineering works, the linear elastic fracture mechanics (LEFM) is proven quite valuable in predicting the crack growth life, which is the predominant part for the whole fatigue life of welded joints on OSDs [9] since the weld defects (e.g. initial cracks and residual stresses) are nearly inevitable and the crack initiation life is significantly shortened. In addition, it may provide a practical use for

* Corresponding author.
 E-mail address: a.chen@tongji.edu.cn (A. Chen).

actual bridges due to the advantage of evaluating the remaining life of OSDs based on fatigue-oriented inspections.

Given the intrinsic feature of fatigue, however, the crack growth that passes through different scales has to be considered. With the tiny initial cracks in welded joints compared with the size of the structure itself, the multiscale problem is one of the biggest obstacles when investigating the fatigue crack growth of OSDs. Generally speaking, a concurrent or semi-concurrent model could achieve results that are more realistic [10–12], as the coupling effects between various scales are considered. But on the issue of fatigue on large-scale engineering works, concurrent models are quite difficult to put into practice because of the huge difference in scales and the consequent computational ability it requires. Therefore, a non-concurrent way seems to be a better option when the trivial coupling effects between the cracked part and the whole structure can be neglected. In that case, the multiscale problem becomes a scale transition problem, and many efforts have been done by considering the micro-/meso-scale features using homogenization method to modify the constitutive model and/or the material properties, [13,14], or using hierarchical models with transitional functions [15,16]. It should be noted that these multiscale models are proposed for various issues and non-universal, and a specific multiscale model for fatigue crack growth of OSDs should be carefully established and validated.

Given the fatigue test designed for the rib-to-deck welded joints of OSDs with beach mark method [17], this paper presents the analysis on the fatigue behavior in the entire process and establishes the multiscale FEA model to apply fracture mechanics on this issue. The remainder of this paper is organized as follows. Section 2 gives a brief description of the fatigue test using the beach mark method that enables to trace the crack. The fatigue behavior analyses on the specimens in the test are then provided, and the whole fatigue process is demonstrated in Section 3. Afterwards, the multiscale model is established in a non-concurrent way using the eXtended Finite Element Method (XFEM) in Section 4. With the multiscale model, the different stages of the fatigue process of the rib-to-deck joint of OSDs are analyzed by crack growth rate (CGR) with respect to the stress intensity factor (SIF) in Section 5. In Section 6 the conclusion is drawn for the final step.

2. Fatigue test

Fatigue test is always regarded as the most convincing way to study the fatigue behavior of OSDs. However, the majority of existing test results are based on the classical stress-life relation, i.e. the S-N curve, which is not so valuable when looking into the entire process of fatigue crack growth and the fatigue mechanism. Therefore, a test designed with easy access to fracture mechanics analysis is quite needed to better understand the entire fatigue process.

A brief introduction is given in this section, while more details can be found in [17].

2.1. Test scheme

As previous studies often obtained scattered results from fatigue tests, it is preferred that the test can be repeated as many times as possible. In that case, a test specimen that consists of several longitudinal stiffeners and at least two crossbeams (as in [18,19]) is not an option for cost concerns. Hence, the test specimen was designed as a small part of OSD around the rib-to-deck welded joint, which consisted of one trapezoidal stiffener and the deck plate, as shown in Fig. 1. The specimens were manufactured using the common steel type of S355, and welded by submerged arc welding according to the common way of OSD production to keep the similarity of the weld defects and residual stresses to the as-welded structures in the reality.

With this design of specimen, extra attention should be paid to the boundary conditions. By comparing several test setups, the boundary conditions are determined with consideration of the implementation in

the laboratory while keeping the similarity of the stress situation as a reference model [17]. Eventually, the boundary conditions are as follows: the specimens are simply supported at a distance of 300 mm to the concerned rib-to-deck welded joint, and fixed on the other side. The load is a line load applied at a distance of 70 mm to the rib-to-deck welded joint. According to the boundary conditions and applied loads, it is expected that the stress will be higher at the weld toe than the weld root. As can be expected, the stress/strain gradients near them are both quite high, and the strain gauge chains are installed to collect the data around in a spacing of 2 mm. The summary of the strain gauge locations is given in Fig. 1. According to the positions, they are numbered in four categories, i.e. TD (the top of deck plate), BD (bottom of deck plate), TS (top of stiffener) and BS (bottom of stiffener).

To understand the fatigue crack growth, beach marks on the fracture face offers a simple way to trace the entire process. According to some of the fatigue tests on OSDs using constant amplitude cycles [19,20], however, the obtained beach marks are either in limited quantities or can hardly be identified visually. Hence, the applied loading sequences are designed to produce up to ten beach marks. It consists of two parts, i.e. the base cycles and the beach mark cycles, with the beach mark cycles being determined according to the following principles,

(1) The maximum load of a beach mark cycle equals that of a base cycle, in order to prevent the effect of overload retardation;
(2) The load range ratio between beach mark cycles and base cycles, μ, is about 0.2–0.4;
(3) The beach mark cycle count should be proper when compared to the base cycle count, so that the beach marks will not be too small to observe;
(4) The number of beach marks will be limited to ten due to the concern for the fatigue test duration.

2.2. Test results

Eleven specimens were tested in total. Among them, ten were applied by two types of load cycles, i.e. the base cycles that lead to the fatigue damage and the beach mark cycles that to produce beach marks. The results show that the crack at the weld toe is predominant in every specimen. The cracks propagate vertically through the deck plate and longitudinally along the weld bead, as shown in Fig. 2. On the other hand, weld root crack is not observed at all, even though it is believed to be more common on real bridges [20]. The summary of the applied loads and cycles till failure for all test specimens is given in Table 1. The parameter μ is given to indicate the ratio between the stress amplitudes induced by these two types of cycles. P_{max} is the maximum loading of the base cycles, and P_{min} is the minimum one. The number of the base cycles is noted as N_{base}, and that of the beach mark cycles is noted as $N_{beachmark}$.

As for the beach marks, Table 1 indicates that nine of the specimens produced beach marks, while the exceptions are Specimen 2 which did not apply beach mark cycles and Specimen 8 which stopped after more than 1.5 million cycles as no sign of failure occurred. It should be noted that due to the lack of experience and reference in using the beach mark method in fatigue tests on OSDs, some attempts are inevitable to find the best way to tune the beach mark technique during the test. Eventually, the specimens with the best quality beach marks are Specimen 7 and Specimen 10, as the final two for the test. As they were the result of the same loading (31 kN, $R = 0$), the results would be comparable. Based on the beach marks, the fatigue behavior is analyzed for the next step.
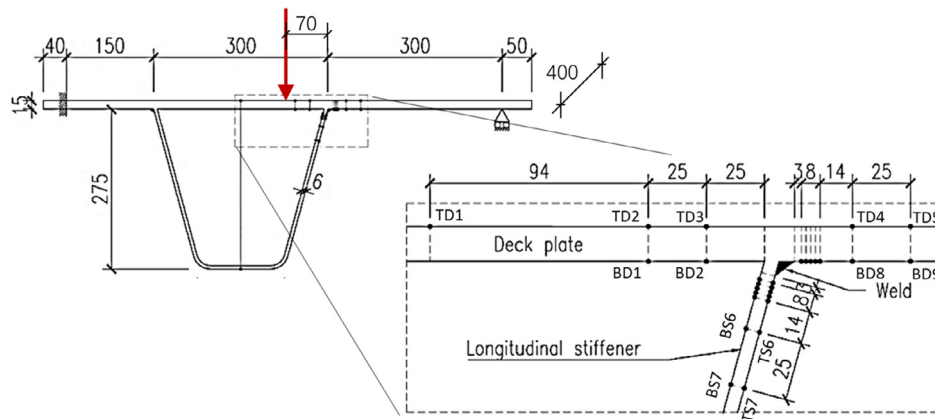
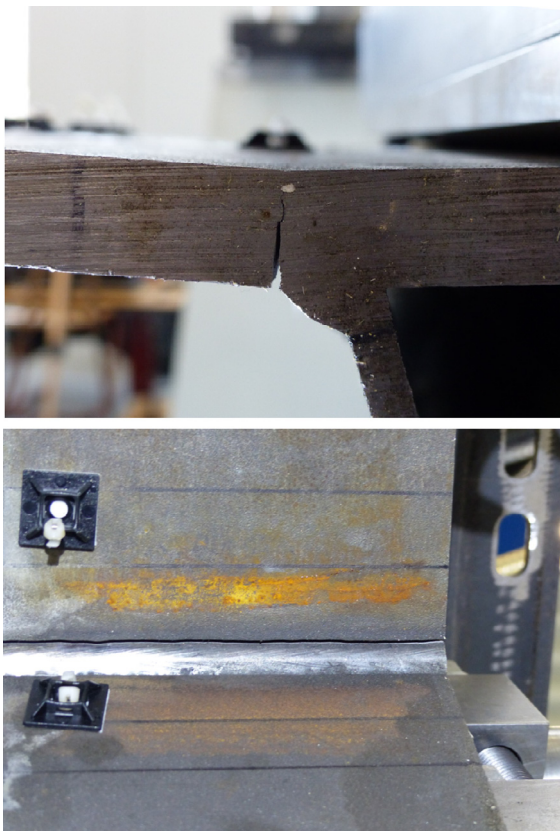**Fig. 1.** Test scheme and the layout of strain gauges (unit in mm).

Fig. 2. Fatigue crack at the weld toe (Specimen 7).

3. Fatigue behavior analysis

3.1. Crack initiation analysis

The obtained beach marks provide a general information about the crack initiation site on the fracture face. Thus, micro- and/or meso-scale observation can easily be conducted for analyzing the crack initiation, as well as the fatigue behavior in other stages. With regard to that, various equipments were applied, including an optical microscope Carl Zeiss Jena Neophot 32, a stereomicroscope NIKON SMZ 800, a scanning electron microscope (SEM) TESCAN VEGA 5130 SB with energy dispersive spectroscopy (EDS) Bruker Quatanax 200.

By observing the fracture face of each specimen, the crack initiation zone can be defined with respect to the different roughness that leads to a visible boundary, as shown in Fig. 3. The most important observation in this zone is the intergranular fracture, as shown in Fig. 4. A typical example on Specimen 10 is given by Fig. 4(c), in which the areas pointed by arrows are the places of fracture. It is believed that the brittle fracture in a small, local area, i.e. the coarse-grained heat-affected zone (HAZ), is the cause of this phenomenon [21], and consequently the cause of crack initiation. Even though the actual fatigue life until the occurrence of intergranular fracture cannot be determined by the test, it is reasonable to assume a negligible cycle count due to the small crack initiation life for OSDs [9]. Therefore, the initial crack depth for each specimen is obtained by measuring the maximum depth of the intergranular fracture, which is mainly around 0.3–0.4 mm, as shown in Table 1. Though slightly different from the real case, it provides the necessary condition for conducting fracture mechanics analysis in the next sections, and will only cause small errors on the first data point when achieving the CGR curve in the following sections.

Table 1
Summary of fatigue test results.

No.	P_{max} (kN)	P_{min} (kN)	μ	R	Initial crack depth (mm)	N_{base}	$N_{beachmark}$
1	27	−27	0.3	−1	0.481	156 535	119 220
2	40	−40	/	−1	/	62 844	/
3	40	−40	0.2	−1	0.379	46 737	168 692
4	0	−40	0.4	0	0.498	147 425	19 500
5	0	−27	0.4	0	0.362	484 782	178 149
6	0	−35	0.4	0	0.282	247 762	99 067
7	0	−31	0.4	0	0.375	272 852	337 525
8	40	0	0.6	−∞	/	> 1 527 492	640 000
9	40	−40	0.4	−1	0.284	40 809	24 402
10	0	−31	0.4	0	0.288	270 544	307 902
11	30	−30	0.2	−1	0.308	101 394	148 871
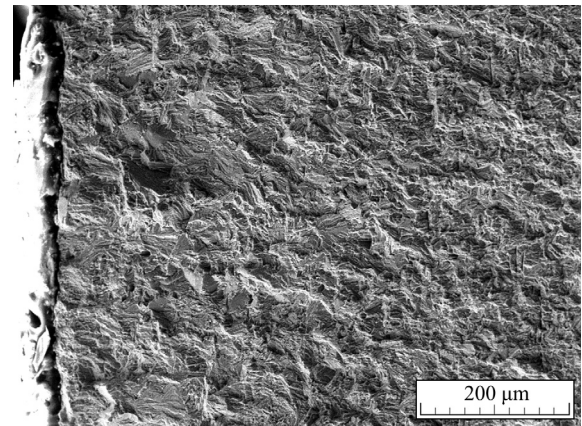
Fig. 3. Different fracture behavior (Specimen 5).
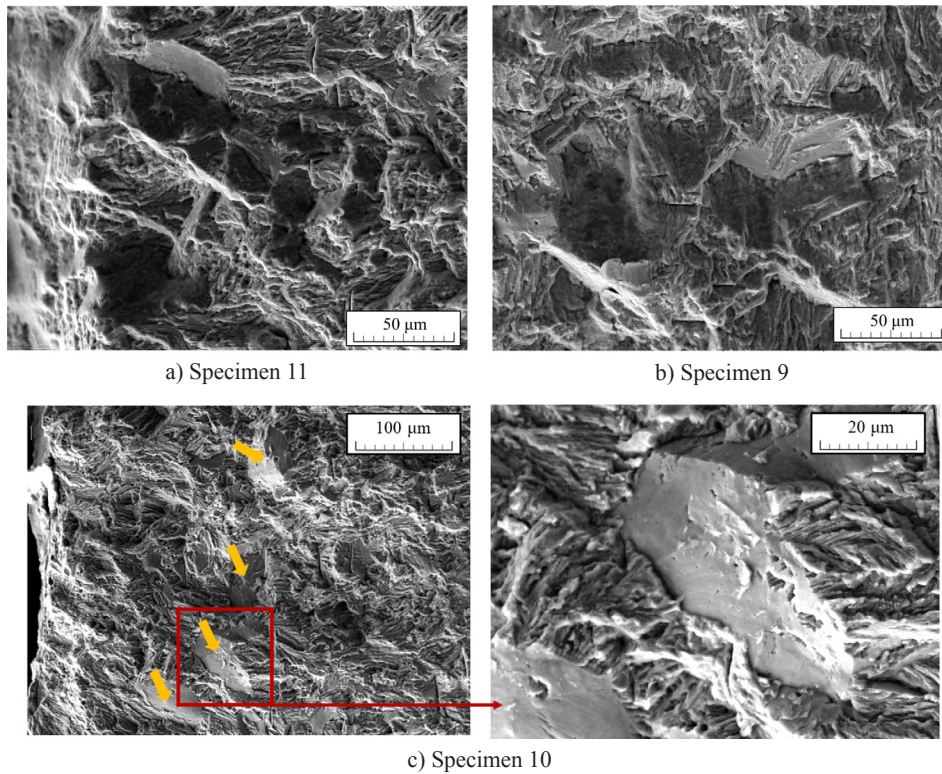
a) Specimen 11

b) Specimen 9

c) Specimen 10

Fig. 4. Intergranular fracture on the fracture surface.

3.2. Crack growth analysis

Outside the crack initiation zone, the beach marks can be used to trace the crack growth process with the crack paths they have presented on the fracture face. Fig. 5 shows the development of the crack depths for each specimen by measuring the beach marks. Basically, the last few beach marks can be observed with the naked eye. The two test specimens with the most beach marks are quite representative, i.e. Specimen 7 and Specimen 10 as shown in Figs. 6 and 7, respectively. According to the visible beach marks, it can be addressed that the crack may initiate at the quarter point or in the middle, and the shape of a single crack is basically semi-elliptical, though there are cases with two main cracks that coalesce together.

However, the first few beach marks can only be identified from a magnified local view from SEM and/or stereo microscope, thus only the

crack depth can be measured. In addition, these beach marks are sometimes discontinuous due to the randomness of the microstructures near the weld toe, which makes it difficult to determine the actual shape of the early-stage cracks. It is logical to assume a semi-elliptical shape with respect to the presented beach marks. But it has to be noted that the aspect ratio of the semi-ellipse a/c (i.e. the crack depth a over the half crack length c) should be much smaller, since the crack initiation caused by the intergranular fracture in the coarse-grained HAZ tends to be uniformly distributed along the longitudinal direction if an ideal line loading is applied.

Even for the beach marks that are visible in a global view, the measurement of the crack length is more complicated due to the crack initiation behavior. As clearly shown in the red-circled part in Fig. 7, the longitudinal end is extended by the coalescence of the main crack and the secondary cracks. Due to the intergranular fracture in the crack initiation zone, these secondary cracks will always initiate along the longitudinal direction and keep coalescing with the main crack. As a consequence, the ideal crack shape in this fatigue test is a semi-ellipse with a smaller aspect ratio than other studies with local loading [19,20], as shown in Fig. 8. When put into practical use for OSDs, the shape should be more approximate to the realistic one, as the fatigue cracks are resulted by moving wheels.

By the above analysis on the shape of beach marks, three steps should be addressed for the fatigue process in this test as well as for a realistic OSD.

(1) A number of tiny cracks initiated because of the intergranular fracture in coarse-grained HAZ.
(2) Cracks grow and coalesce with each other till a main crack forms.
(3) The main crack grows vertically by the driving force from the SIFs and longitudinally due to both the SIF driving force and more importantly, the consecutive crack coalescence.
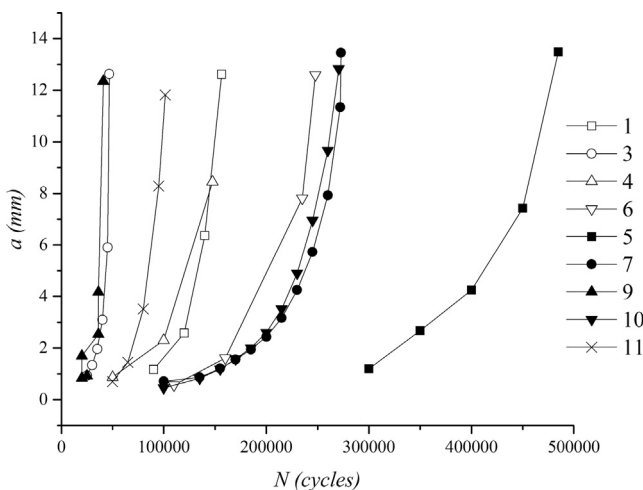

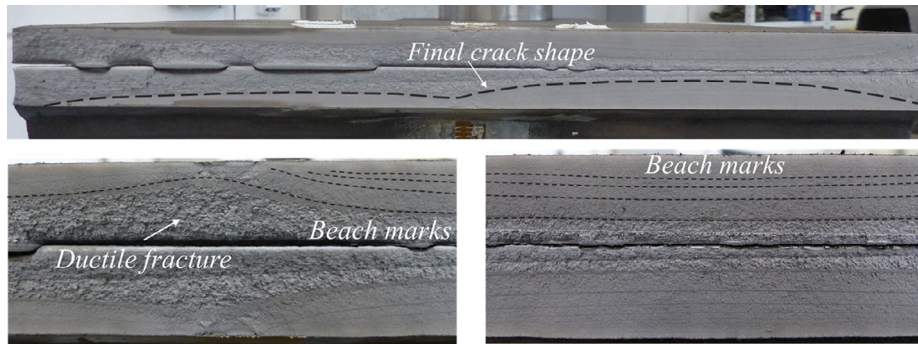**Fig. 5.** The crack growth according to the beach marks.

Fig. 6. Beach marks on Specimen 7.

3.3. Application of Paris law for the crack development

Due to the aforementioned difficulty in determining the accurate crack depths and lengths, an equivalent way is applied based on the principles given by the IIW recommendations [22]. For the first step, the lengths of visible beach marks are roughly measured in a precision level of 0.5 mm, which would lead to negligible errors given that the length is large enough. If two main cracks can be distinguished clearly, the length is determined to be the summary of both lengths, and the depth is the maximum one. As a result, the equivalent semi-elliptical crack face can be obtained. Fig. 9 demonstrates the way by giving Specimen 7 as an example.

As for the first few beach marks near the initial crack zone, this equivalent way shows its incapability because of the unmeasurable crack length. To solve this, a damage-based method is put forward to fit the crack lengths using measurable data, i.e. the crack depth.

Assuming that only one main crack exists in the specimen, the applied fatigue cycle, N_{app}, will introduce damages, D, by enlarging the area of it, i.e.

$$N_{app} \propto D \propto Area \tag{1}$$

As mentioned before, the crack growth in the depth is dominant by SIFs and thus fracture mechanics can be introduced,

$$\frac{da}{dN} = C\Delta K^m = C[F\Delta\sigma\sqrt{\pi a}]^m \tag{2}$$

hence,

$$N_{app} = \int dN = \int \frac{da}{C[F\Delta\sigma\sqrt{\pi a}]^m} \propto Area \tag{3}$$

It gives the relationship between the measurable crack depth and the crack area, though a full-analytical expression is not available due to the unknown shape factor, F. Based on that, a hypothesis can be put forward that the crack area varies with the crack depth in accordance

with the power law,

$$Area = p_1 a^{p_2} \tag{4}$$

With all the large beach marks whose length and depth are measured, the data is fitted to get the value of coefficients p_1 and p_2, as shown in Fig. 10. By introducing the area formula for semi-ellipse to Eq. (4), the aspect ratio can be obtained by

$$a/c = \pi a^{0.837}/360.2 \tag{5}$$

It is worth to mention that the fitting excludes all specimens under load ratio of -1. The reason is partly that the first few beach marks are barely seen on these specimens even in microscopes. More importantly, even there are a few distinguishable ones, they always grow to the longitudinal end of the specimen as the fatigue load is more aggressive. Therefore, the shape should not be considered as semi-elliptical anymore, and the behavior is believed to be different as well. In the same manner, the validation of the multiscale study in next sections is carried out with respect to the specimens under load ratio of zero only.

4. Multiscale FEA models

4.1. Macroscopic model

For the first step, a macroscopic model consisting of 419 380 solid elements is built in finite element software SAMCEF with respect to the fatigue test setup [17], as shown in Fig. 11(a). With respect to the effect of the local toe geometry to the small cracks, the flank angle is considered the same as the test specimens. However, due to the manufacturing, the flank angle measured on several sections of the specimens is not consistent (around 37–45°). The flank angle is then set to be 40 degrees. The realistic boundary conditions are simulated as precisely as possible. With the eXtended Finite Element Method (XFEM) module in SAMCEF, a user-defined XFE domain that contains a crack can be defined in the model. The mesh around the crack will have to be refined to
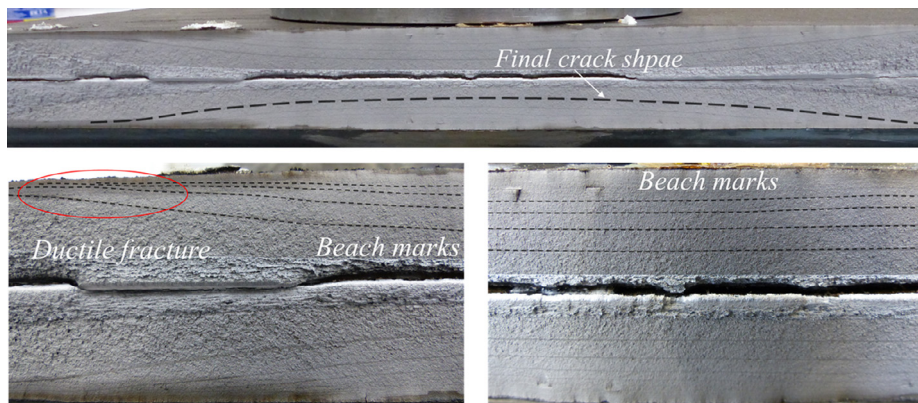

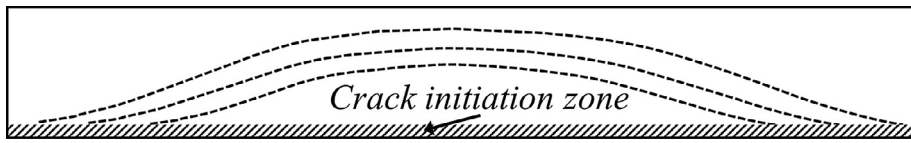**Fig. 7.** Beach marks on Specimen 10.

Fig. 8. The ideal shape of the crack with consideration of merging of initial cracks.

generate sufficient elements to calculate the SIFs along the crack front, while largely increases the computational intensity. In addition, the contact functions defined for the boundary conditions push it to a more difficult scenario. Hence, it is used as a benchmark model with no cracks embedded inside.

Therefore, another model is built with the simplified boundary conditions, as shown in Fig. 11(b), for which a coarser mesh is used to reduce the total element number to 144 966. The boundary conditions are simplified, i.e. fixing the deformation of the specimen on all directions on the left, and the deformation on the longitudinal and vertical directions on the simple-supported line on the right, exactly as given in Fig. 1. With consideration of the non-uniform load distribution on the specimen due to the deformation of the loading bar, the applied loading is defined by reading the contact force in the previous model. The sensitivity check on the simplified model is conducted, showing a great consistency to the benchmark model as the maximum displacement is slightly reduced by less than 1% (from 5.04 mm to 4.99 mm). The simplified model is thus validated and will be used in the following studies, noted as SAMCEF model hereinafter.

Ideally, the fatigue test process will be reproduced by the SAMCEF model if the cracks that are corresponding to the beach marks are introduced. After attempts on inserting all cracks, however, it turns to be feasible for those with the depths larger than 1.5 mm only. When an early-stage crack is inserted, the computation is too heavy since the shallow but long crack shape requires a large XFE domain with a high mesh density. Given that the XFEM has already provided the advantage by allowing the crack body to intersect the elements, the mesh is basically dependent on the requirement of stress field around the crack front, and refinement of it is hard to be further optimized.

It therefore implies the necessity to establish a multiscale way on this issue, especially aiming at the early-stage cracks whose depth can be as small as 0.2 mm. Fortunately, as the aspect ratios for early-stage cracks are quite small, the crack length is much larger than the depth, which means the stress field for the crack front could be approximated by plane strain assumption in two-dimensions. On the other hand, the sizes for these early-stage cracks are not too small to go into the microscale which is dominated by microstructural mechanics. Therefore, it is possible to solve these mesoscopic cases based on LEFM and the XFEM program developed in MATLAB [14,23]. Eventually, two kinds of two-dimensional model with respect to multiscale concerns are built: (i) displacement-based sub-model; (ii) stress-based local model.

4.2. FEA sub-model

To study the early-stage cracks, a sub-model method is adopted in the first place. By introducing the displacements extracted from the SAMCEF model to a sub-model, the feasibility of the computation can be improved when compared to a completely-refined model.

For the first step, the SAMCEF model is modified by cutting out a small region, and the sub-model is built accordingly, as shown in Fig. 12. With respect to the size of cracks to be analyzed, its dimension is set to be 2 mm × 2 mm (the length due to the flank angle is not included). A fine mesh with an element length of 10 μm is used, lead to more than 40,000 elements in the sub-model. The sub-model will be applied by forced displacement boundary conditions, which can be interpolated according to the nodes on the SAMCEF model, i.e. the blue-dotted ones in Fig. 12(b). It should be noted that the boundary conditions for such a two-dimensional model will have to be linked to one cross-section of the SAMCEF model. For the conservative reason, it is selected to be the one at the deepest point of the crack front, and will surely exaggerate the displacements on the boundaries.

To verify this method, cases with different crack depth, *a*, and half-length, *c*, are solved by both the SAMCEF model and the sub-model. For instance, the crack noted as *a0.3c3* refers to a crack with a depth of 0.3 mm and a half-length of 3 mm. Firstly, four cases, i.e. *a0.3c3*, *a0.3c5*, *a1c10*, *a1c20*, are compared. The stress field around the crack tip for the case of *a0.3c3* is given in Fig. 13 as an example. The obtained SIFs are given in Table 2, in which the results obtained by sub-model are always much larger than that by SAMCEF model. The reason is, as mentioned before, that the forced displacements on boundaries are actually exaggerated. When comparing the cases of same depth but different length, i.e. *a0.3c3* against *a0.3c5*, and *a1c10* against *a1c20*, the difference is minor, which implies that the difference caused by the plane strain assumption could be negligible when the crack is long enough.

Afterwards, for some beach marks that are able to analyze by both the SAMCEF model and the sub-model, the accuracy of the sub-model is checked. Hereinafter, the beach marks are noted by both specimen number and beach mark number. For example, S10BM4 refers to the 4th beach mark identified on Specimen 10. Results from three beach marks are compared, i.e. S10BM4, S7BM4, S6BM2, as shown in Table 2. It can be seen that the differences are always around 5%, which are small but still noticeable.

To summarize, this displacement based sub-model could achieve solutions in case the plane strain assumption is applied reasonably. But after all, the sub-model is only a refined model of the macroscopic one. By any means, the results are largely dependent on the SAMCEF model, which is proven not capable of solving cases for early-stage cracks. The errors are also inevitable due to the essential difference between the two-dimensional sub-model and the three-dimensional SAMCEF model.
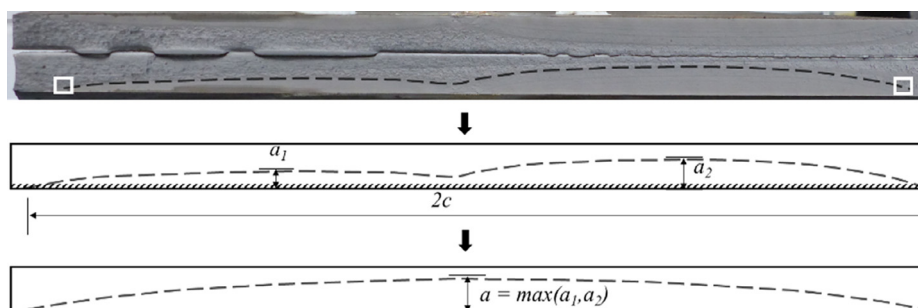

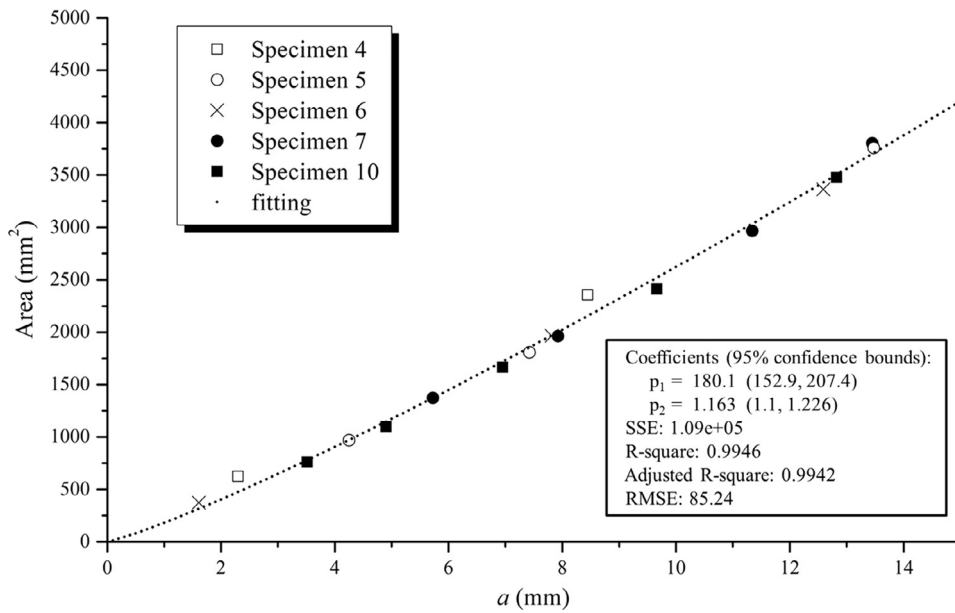Fig. 9. The equivalent semi-elliptical crack on Specimen 7.

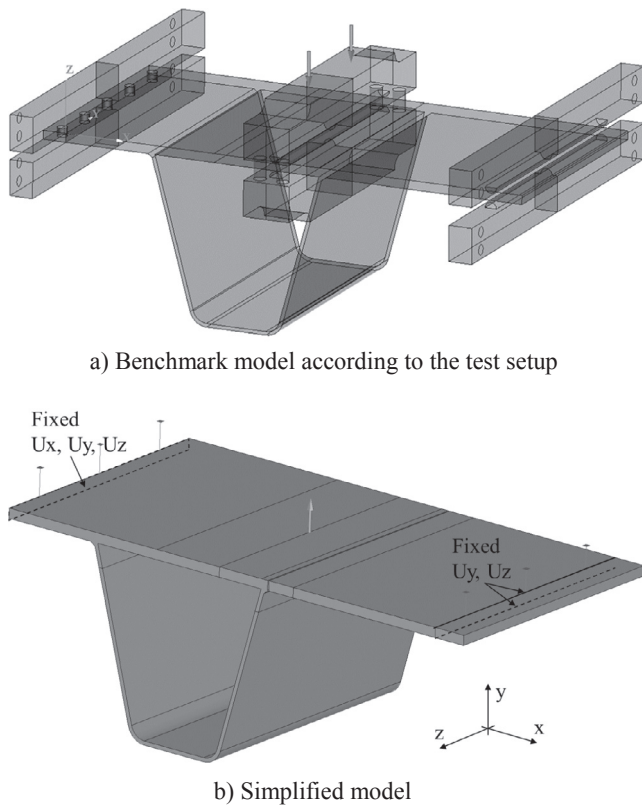**Fig. 10.** The curve fitting on the crack area varies with the depth.

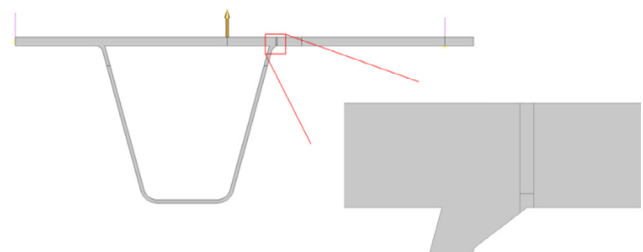a) Benchmark model according to the test setup

b) Simplified model

Fig. 11. Macroscopic model in SAMCEF.

a) The cutout on the SAMCEF model

b) The boundary nodes of sub-model
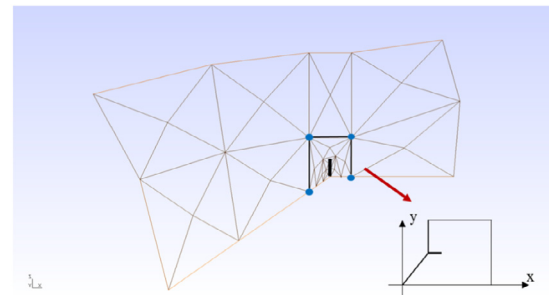
Fig. 12. The sub-model based multiscale method.

Furthermore, the efficiency of this method is not preferred due to the lack of program interface between the macroscopic model in SAMCEF and the sub-model in MATLAB.

4.3. Local FEA model

Since the disadvantages of sub-model is mainly due to its dependency to the macroscopic model, a local model is put forward in a non-concurrent and independent way. It enables to calculate SIFs with a similar concept as the classical nominal stress way, which will be preferred in terms of both feasibility and efficiency.

Firstly, a two-dimensional model with an initial crack, referred as the local model hereinafter, is built with respect to the full thickness of the deck plate, as given by Fig. 14. The boundary conditions in the local model are a full fixation of the left edge and application of the bending/membrane stresses on the right edge. In most cases for OSDs, the membrane stresses are so small that can be ignored, and only the bending stresses are applied to the local model [23].

The SIFs for cracks with depths ranging from 0.1 to 0.5 mm are calculated using the local model, by applying a bending stress of 100 MPa, as shown in Fig. 15. The results will be used as a standard case later. The SIF for mixed mode crack can be obtained by the following equation [24].

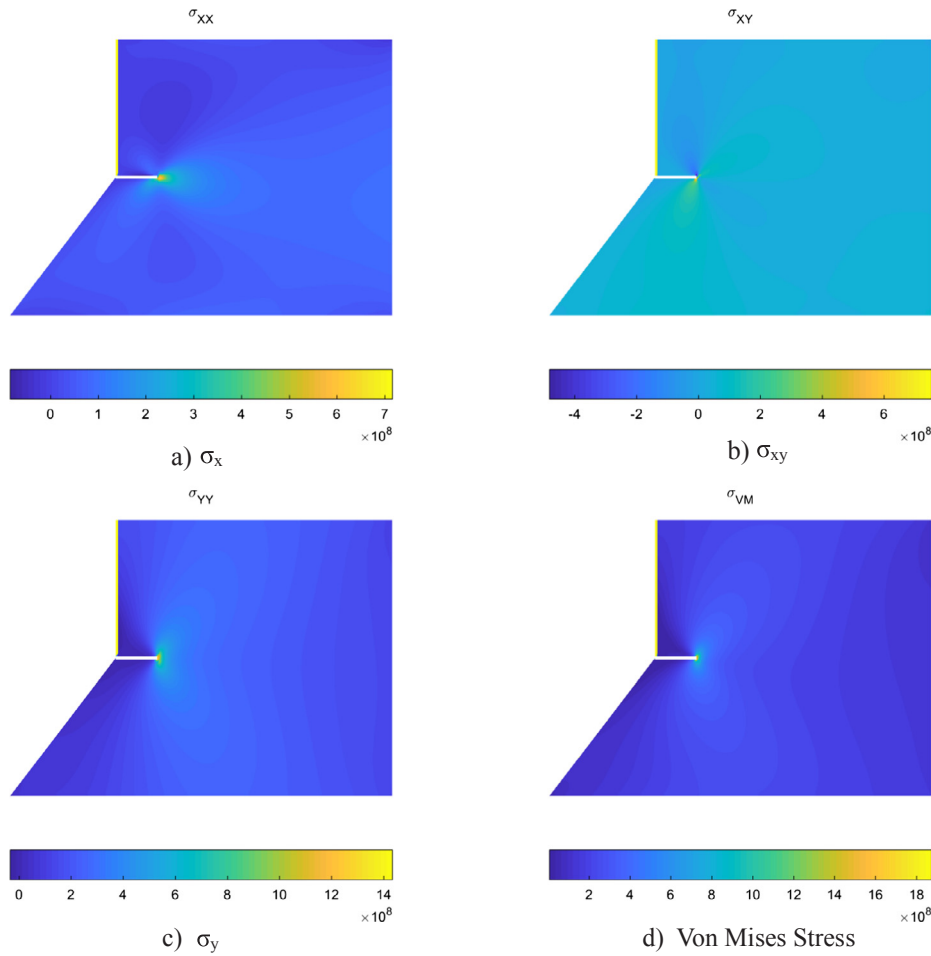$$K_{eff} = \sqrt[4]{K_I^4 + 8K_{II}^4} \tag{6}$$

Fig. 13. Stress field on a weld toe (corresponding to the bold part in Fig. 12, unit in Pa).

Table 2
Verification of results obtained by sub-model.

Crack	Crack dimensions		SIF (MPa √m)		Diff.
	a (mm)	c (mm)	sub-model	SAMCEF	
a0.3c3	0.3	3	10.03	8.6	16.66%
a0.3c5	0.3	5	10.28	8.87	15.89%
a1c10	1	10	13.46	11.73	14.75%
a1c20	1	20	13.84	12.15	13.87%
S10BM4	1.578	123.510	15.15	14.31	5.90%
S7BM4	1.551	123.158	14.87	14.15	5.12%
S6BM2	1.611	147.500	17.05	16.26	4.89%

Nevertheless, K_{II} is often much smaller than K_I in this case, and the biquadrate in Eq. (6) even made it negligible. Hence, the effective SIF generally varies with K_I only.

Two benchmarks are given to validate this local model by comparing the Mode-I SIFs, as shown in Fig. 16. To be comparable with the SIFs obtained by stress intensity factor handbook [25] and Newman-Raju Equation [26], the local model is firstly built without considering the flank angle, as shown in Fig. 16(a). The SIFs presented for Newman-Raju Equation are the results at the deepest point of a crack with an aspect ratio of 0.01, which makes it quite close to the plane strain status. It can be seen that the adopted boundary conditions agree with the existing studies that using nominal stress, as long as the boundary is far away enough from the crack. In case that the flank angle is considered, the distance between the crack and boundaries, *w/2,* should be further verified. Assuming a flank angle of 40°, a set of local models with various values of *w/2* are built and compared, as shown in

Fig. 16(b). Due to the stress concentration, the bending stresses on the boundaries for different cases are determined accordingly. The obtained SIFs are quite close when *w/2* is larger than 5 mm, indicating the small error using this local model.

Hence, this local model is used to calculate the SIFs for beach marks of early-stage cracks. Note that the model is valid when the crack is small enough, so that the bending stress ranges, as the boundary condition, will keep unchanged as the nominal stress. In that case, the bending stress ranges to be applied should be determined and verified properly. The strains measured in the fatigue test of Specimen 10 at different positions are shown in Fig. 17, in which the smaller strain ranges can be easily distinguished as beach mark cycles. The strain ranges before the *i*-th beach mark, ($\Delta \varepsilon_i$ defined in Fig. 17a) can be compared. Table 3 provides the strain ranges at different gauges till the 4th beach mark, which refers to the crack in a depth of 1.578 mm. It can be addressed that the change of the strain range is almost negligible, i.e. only 2.75% for Strain Gauge BD7 (*w/2* = 11 mm) and 3.82% for Strain Gauge BD6 (*w/2* = 9 mm). Hence, the bending stress to be applied can be obtained by reading the stress in the SAMCEF model at the corresponding position. Consequently, *w/2* is set to be 8 mm with respect to the crack sizes. That gives the dimension of the local model being 16 × 15 mm. As it is much larger than the sub-model, the element size of 20 μm is adopted for the sake of computing efficiency, leading to more than 600,000 elements.

In the same manner as the sub-model does, the results of the early-stage beach marks are compared with those calculated by the SAMCEF model. Again, the results of three beach marks, i.e. S10BM4, S7BM4, S6BM2, are compared, as shown in Table 4. Clearly, the local model often obtains results that are slightly smaller than that from the
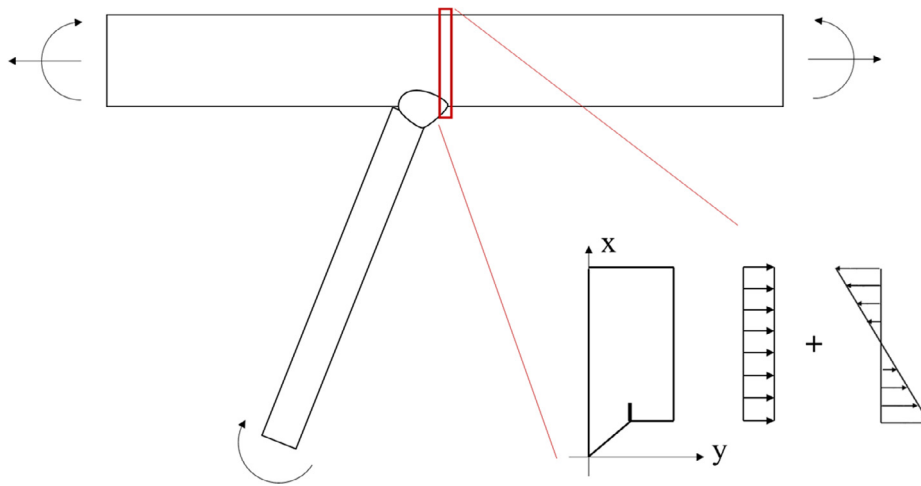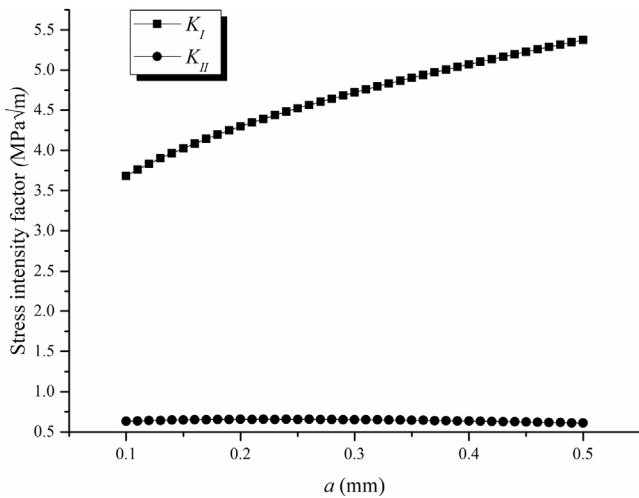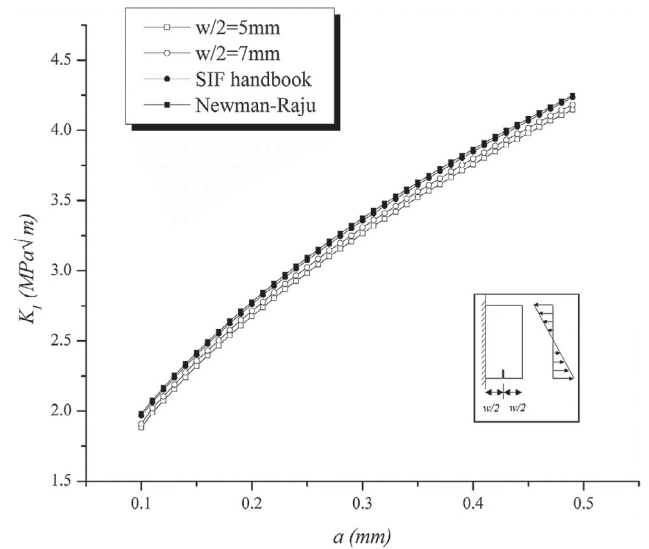
Fig. 14. The scheme of the local model.

Fig. 15. Stress intensity factors under bending stress of 100 MPa.

a) without the flank angle
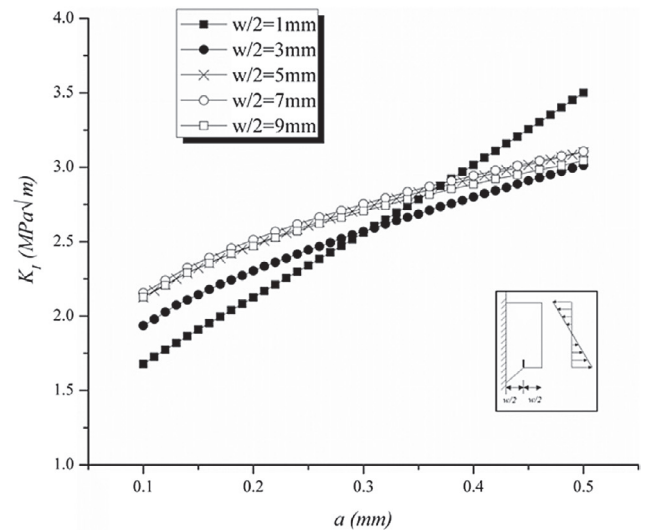
b) with the flank angle

Fig. 16. Validation of the local model.

SAMCEF model. It should be attributed to the boundary conditions that underestimated the stress concentration effect caused by cracks. It is also the reason that this model is not applicable to cases of cracks with large sizes. When compared to the results in Table 2, the better agreement indicates that the local model is more suitable than submodel on this issue. Furthermore, the efficiency is largely increased as being non-concurrent and independent to the SAMCEF model. Therefore, the combination of the local model and the SAMCEF model forms a feasible and accurate way to calculate the SIFs for all beach marks in the test.

5. Fatigue process analysis

5.1. Methodology for determining the fatigue process

By conducting the above works, the fatigue test on rib-to-deck welded joint of OSD can be analyzed with respect to the entire process that the initial crack at the weld toe grows till the structure failure. Fig. 18 presents the flowchart of the fatigue process analysis.

For the first step, the beach marks on the specimens demonstrate the crack growth rates, as well as the general shapes, depths, and lengths of cracks. Additionally, the fractographic analysis in micro-scale indicates the depths of initial cracks, while the shapes and lengths of them are hypothetical based on the measurable beach marks. The multiscale solution using the macroscopic SAMCEF model and the mesoscopic

a) Strain gauge BD7 (*w/2* = 11 mm)

b) Strain gauge BD6 (*w/2* = 9 mm)

c) Strain gauge BD5 (*w/2* = 7 mm)

d) Strain gauge BD4 (*w/2* = 5 mm)

e) Strain gauge BD3 (*w/2* = 3 mm)
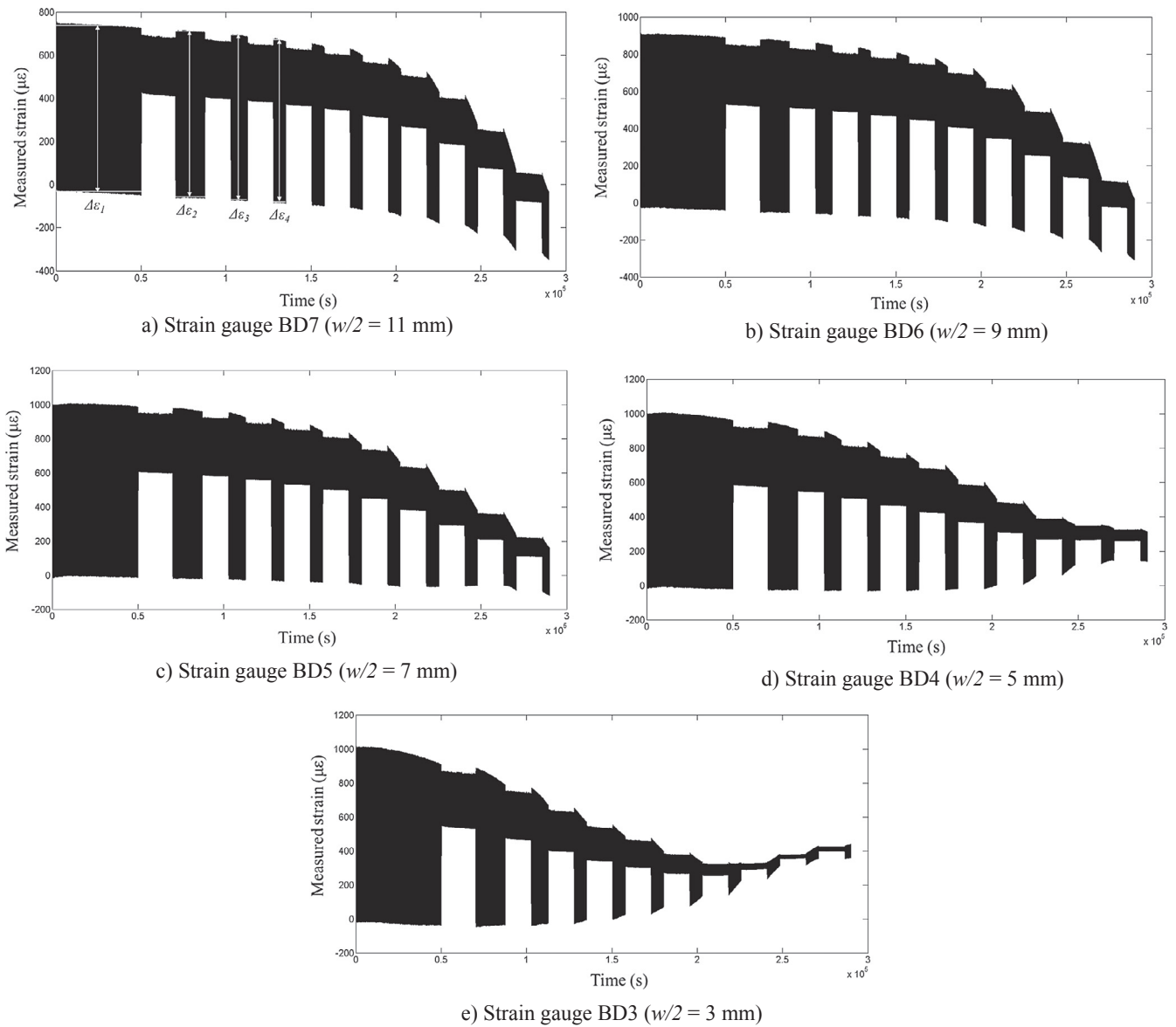
Fig. 17. Time history of strain measured for Specimen 10.

Table 3
The reductions of strain range at different strain gauges.

Strain gauge	$w/2$ (mm)	$\Delta\varepsilon_1$ (με)	$\Delta\varepsilon_2$ (με)	$\Delta\varepsilon_3$ (με)	$\Delta\varepsilon_4$ (με)	$(\Delta\varepsilon_4 - \Delta\varepsilon_1)/\Delta\varepsilon_1$
BD3	3	981.134	861.631	738.358	610.268	−37.80%
BD4	5	979.824	934.435	881.065	817.893	−16.53%
BD5	7	984.391	966.775	943.271	913.578	−7.19%
BD6	9	910.794	903.099	891.315	876.024	−3.82%
BD7	11	757.798	753.430	746.284	736.927	−2.75%

Table 4
Verification of results obtained by the local model.

Beach mark	Crack dimensions		K (MPa √m)		Diff.
	a (mm)	c (mm)	Local model	SAMCEF	
S10BM4	1.578	123.510	13.81	14.31	−3.52%
S7BM4	1.551	123.158	13.74	14.15	−2.90%
S6BM2	1.611	147.500	15.70	16.26	−3.46%
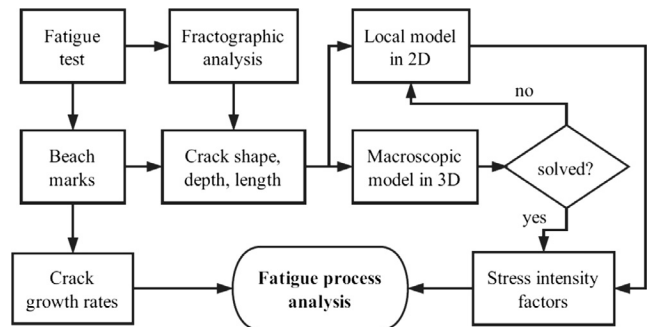
Fig. 18. Flowchart for the fatigue process analysis.

local model provides a numerical way to reproduce the fatigue process for each test specimen. By applying fatigue loads in correspondence with the test, as given by Table 1, the SIF ranges for all cracks in different stages can be achieved consequently.

Following the above procedure, the results are obtained and summarized in Table 5. A few remarks should be addressed to obtain these

Table 5
Summary of calculation on specimens with $R = 0$.

Specimen No.	Beach mark	N	a (mm)	c (mm)	a/c	$\Delta\sigma$ (MPa)	ΔK (MPa·√m)
4	0	0	0.498	102.331	0.005	222.21	13.04
	1	50000	0.874	112.166	0.008	222.21	15.03
	2	100000	2.299	**172.500**	0.013	\	21.29
	3	147425	8.447	**177.500**	0.048	\	44.37
5	0	0	0.362	97.173	0.004	149.99	8.17
	1	300000	1.199	118.098	0.010	149.99	11.07
	2	350000	2.673	134.584	0.020	\	15.23
	3	400000	4.251	**145.000**	0.029	\	18.74
	4	450000	7.425	**155.000**	0.048	\	25.83
	5	484782	13.480	**177.500**	0.076	\	24.05
6	0	0	0.282	93.259	0.003	194.43	9.99
	1	110000	0.561	104.346	0.005	194.43	11.75
	2	160000	1.611	**147.500**	0.011	\	16.26
	3	235000	7.815	**160.000**	0.049	\	35.15
	4	247762	12.591	**170.000**	0.074	\	40.20
7	0	0	0.375	97.724	0.004	172.21	9.45
	1	100000	0.539	103.678	0.005	172.21	10.30
	2	135000	0.863	111.944	0.008	172.21	11.60
	3	155000	1.210	118.273	0.010	172.21	12.74
	4	170000	1.551	123.158	0.013	\	14.15
	5	185000	1.947	127.808	0.015	\	15.44
	6	200000	2.436	132.567	0.018	\	16.66
	7	215000	3.162	138.324	0.023	\	18.66
	8	230000	4.251	145.159	0.029	\	21.51
	9	245000	5.725	**152.500**	0.038	\	25.20
	10	260000	7.925	**157.500**	0.050	\	31.18
	11	272000	11.341	**166.500**	0.068	\	36.61
	12	272852	13.453	**180.000**	0.075	\	29.26
10	0	0	0.288	93.613	0.003	172.21	8.89
	1	100000	0.451	100.699	0.004	172.21	9.87
	2	135000	0.825	111.116	0.007	172.21	11.46
	3	155000	1.188	117.920	0.010	172.21	12.67
	4	170000	1.578	123.505	0.013	\	14.31
	5	185000	2.002	128.390	0.016	\	15.57
	6	200000	2.601	133.987	0.019	\	17.23
	7	215000	3.514	**137.500**	0.026	\	19.65
	8	230000	4.900	**142.500**	0.034	\	23.24
	9	245000	6.952	**152.500**	0.046	\	28.57
	10	260000	9.663	**159.000**	0.061	\	34.60
	11	270544	12.827	**172.500**	0.074	\	32.85

results:

(1) The initial cracks, whose depths are measured according to the intergranular fracture on coarse-grained HAZ, are noted as beach mark No. 0 hereinafter. Besides, the depth is not uniform along the longitudinal direction according to the microscope observation. Therefore, these values could be less accurate, and are noted by gray blocks in Table 5.

(2) For those beach marks with clear longitudinal ends, the lengths are measured with the precision of 0.5 mm, and noted in bolded numbers in Table 5. They are used in the curve fitting in Fig. 10, while the rest ones are calculated in the way proposed in Section 3.3. As a consequence, the aspect ratio for small crack seems quite low as an equivalent value that takes into account the crack coalescence in the initiation zone.

(3) All cases are attempted to solve by the SAMCEF model first, and only the failed ones are then solved using the local model. The boundary conditions for the case solved by local models, i.e. the applied stress ranges, $\Delta\sigma$, are given according to the SAMCEF model as shown in Table 5.

(4) The presented SIF ranges in Table 5 are those at the deepest point of the crack. Nevertheless, it is not necessarily the position of the maximum value along the crack front. Due to the limited size of the specimens, large cracks may lead to evident stress redistribution, and the maximum SIF range could shift from the crack tip to sideways. Hence in some cases, the SIF range of larger crack even tend to reduce, e.g. S10BM10 compared to S10BM11, S7BM11 compared to S7BM12, and S5BM4 compared to S5BM5.

5.2. The crack growth rate curve

While for obtaining the CGR curve, it should be noted that it is achieved by recording the distance between two beach marks and the corresponding cycles, which means it is an average value. Therefore, the SIF ranges for each beach mark cannot be used directly, instead, a representative SIF range for one period is required. As the Paris law indicated, the CGR changes with SIF range in power law, and therefore a linearity can be expected when taking the logarithm of them,

Table 6
Summary of the representative SIF ranges and the corresponding CGRs.

Specimen No.	i	$\Delta a/\Delta N$ (m/cycle)	$\Delta \bar{K}_i$	Specimen No.	i	$\Delta a/\Delta N$ (m/cycle)	$\Delta \bar{K}_i$
4	1	7.525E−09	14.00	5	1	2.789E−09	9.51
	2	2.850E−08	17.89		2	2.948E−08	12.98
	3	1.296E−07	30.74		3	3.156E−08	16.89
6	1	2.540E−09	10.83		4	6.348E−08	22.00
	2	2.100E−08	13.58		5	1.741E−07	24.92
	3	8.272E−08	25.73	7	1	1.641E−09	9.87
	4	3.742E−07	41.18		2	9.261E−09	10.93
10	1	1.628E−09	9.37		3	1.732E−08	12.16
	2	1.069E−08	10.64		4	2.273E−08	13.23
	3	1.815E−08	12.05		5	2.640E−08	14.56
	4	2.600E−08	13.23		6	3.263E−08	16.04
	5	2.827E−08	14.66		7	4.840E−08	17.63
	6	3.993E−08	16.38		8	7.260E−08	20.04
	7	6.087E−08	18.40		9	9.826E−08	23.28
	8	9.240E−08	21.37		10	1.467E−07	28.03
	9	1.368E−07	25.77		11	2.846E−07	33.78
	10	1.807E−07	31.44		12	2.479E−06	32.73
	11	3.001E−07	33.71				

$$log_{10}(\frac{\Delta a}{\Delta N})_i = log_{10}C + mlog_{10}\Delta\bar{K}_i \tag{7}$$

where i refers to the period before the i-th beach mark, $\Delta\bar{K}_i$ is the representative SIF range for this period. Being a linearity, it is easy to get $\Delta\bar{K}_i$ as follows,

$$log_{10}\Delta\bar{K}_i = (log_{10}\Delta K_{i-1} + log_{10}\Delta K_i)/2 \tag{8}$$

where ΔK_i is the SIF range for the i-th beach mark. The results are shown in Table 6.

Consequently, the curve of the CGR, da/dN, against the SIF range, ΔK, can be drawn in logarithm coordinates, as shown in Fig. 19. It can be seen that the results for Specimen 7 and Specimen 10 are in good agreement, as they were carried out by the same loading history. Additionally, results from these two specimens are optimal for further analysis, because they contain the most points among all curves. By contrast, results for Specimen 4 are showing clearly lower CGR than others. It should be attributed to the fitting for crack shape, where Specimen 4 has only two measurable points and thus the least weight in the fitting. As shown in Fig. 10, points for Specimen 4 also seem slightly further away from the fitting curve than other points do.

Afterwards, the different stages in the test can be distinguished by CGR curves. Due to limited points on other specimens, analyses were conducted on Specimen 7 and Specimen 10 only, as shown in Fig. 20. The stages of crack growth can then be elaborated as follows.

Stage I: the initial crack stage, in which the crack growth rate is low but increases sharply. In this stage, the material heterogeneities will
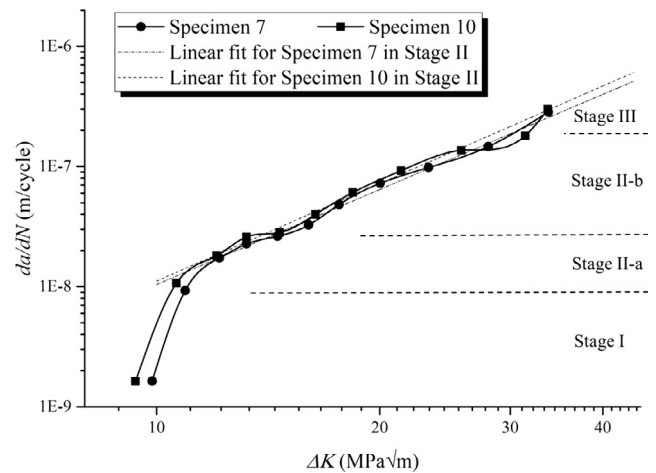

Fig. 19. Crack growth rate for specimens with $R = 0$.

Fig. 20. Typical CGR curves and different stages.

affect the crack growth, and lead to bigger uncertainties than other stages. According to the beach marks, this stage lasts till the crack grows to a depth of about 0.5 mm, which should explain the initial crack size adopted in some literature [27].

Stage II-a: the transition stage, in which the increment of CGR, i.e. the slope of the curve, slows down gradually. In the meantime, the uncertainty induced by the microscopic and mesoscopic heterogeneities gets smaller, since two curves are getting closer to each other. At the end of this stage, as the crack (in a depth of 1.5–2 mm) is getting further away from the HAZ, the reduction of CGR can be identified on the curve. One possible reason could be the fine-grained HAZ that with better fatigue toughness, while it still needs to be confirmed by further studies.

Stage II-b: the stable crack propagation stage. It is the stage that the points of Specimen 7 and Specimen 7 match with each other perfectly. It is not surprising that the classical Paris law can be applied, and the material constants in Paris law can be estimated.

Stage III: the unstable crack propagation stage.

5.3. Material constants estimation

As suggested before, in Stage II-b the crack-tip is away from the HAZ and thus can be assured that crack propagates stably following Paris law. The material constants in Paris law can be estimated by the results, and applied on the prediction of actual welded joints of OSDs. However,
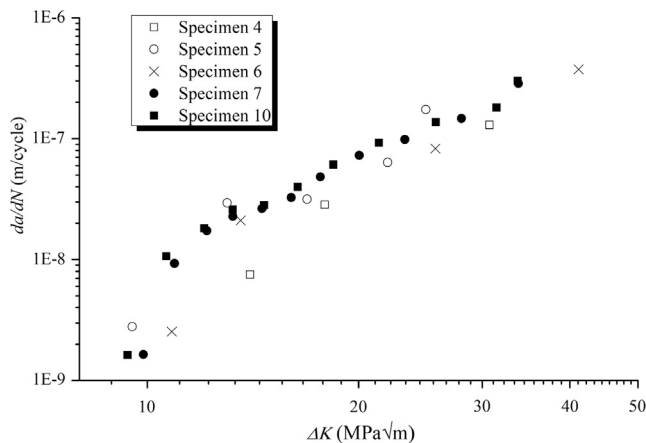
Table 7
Summary of the fittings of material constants.

		Fit 1	Fit 2	Fit 3	Fit 4
Fitting with		Dataset 1[*]	Dataset 1[*]	Dataset 2[*]	Dataset 2[*]
Coefficients	C	8.511×10^{-12}	1.905×10^{-11}	7.943×10^{-12}	2.570×10^{-11}
	95% confidence bounds	$(7.943 \times 10^{-12},$ $9.120 \times 10^{-12})$	$(7.762 \times 10^{-12},$ $4.786 \times 10^{-11})$	$(7.079 \times 10^{-12},$ $8.710 \times 10^{-12})$	$(1.259 \times 10^{-11},$ $5.129 \times 10^{-11})$
	m	3 (fixed)	2.726	3 (fixed)	2.603
	95% confidence bounds	\	(2.419, 3.033)	\	(2.369, 2.837)
Goodness of fit	SSE	0.0225	0.0155	0.3849	0.2657
	R-square	0.9683	0.9782	0.9287	0.9508
	Adjusted R-square	0.9683	0.9758	0.9287	0.9489
	RMSE	0.0475	0.0415	0.1172	0.0992

[*] Dataset 1 refers to the points in Stage II-b for Specimen 10 & 7, and Dataset 2 refers to the points excluding Stage I for all specimens.

it is not hard to notice that most of the data points, except those in Stage I, can be interpreted by Paris law as well, despite the effect of HAZ to CGRs. In that case, two different datasets, i.e. Dataset 1 and Dataset 2, are adopted in the fitting to estimate the material constants. The former one refers to the points in Stage II-b for Specimen 7 and Specimen 10, while the latter refers to the points for all specimens by ignoring those in Stage I. Additionally, as recommended by most of the literature, such as the IIW recommendation [22], BS 7910 [28], the value of Pairs exponent, m, can be set to three with confidence. To be comparable, fittings are carried out based on m equals three or the fitted value. Hence, four groups of fittings, named as Fit 1, 2, 3 and 4, are given in Table 7.

Based on Eq. (7), the curve fitting toolbox in MATLAB is applied to obtain the fitted values of the material constants, as well as the parameters illustrating the goodness of the fitting. The results are shown in Table 7 and Fig. 21. According to the results, it can be seen that the fittings with Dataset 2 (Fit 3 & 4) are quite close to those with Dataset 1 (Fit 1 & 2), even though the parameters, such as the sum of squared errors (SSE), R-square, and root mean square errors (RMSE), shows better fitting quality for Dataset 1. As a result, it can be concluded that Fit 3 and 4 provides the material constants that are applicable to most parts of the crack growth process with acceptable errors in fatigue life estimation. It would be quite favored by the actual projects for the sake of simplicity. When comparing the results without fixing m (Fit 2 & 4) to those with fixed m (Fit 1 & 3), the former ones, as can be expected, show slightly better fitting qualities.

Table 8 presents the best fitted material constants (Fit 2) compared with those from the literature. It is clear that the values of Paris constant C_2 are quite close to each other. Note that the differences of Paris constant C_2 are calculated in logarithm coordinates, in accordance with how it is estimated using curve fitting. The differences in Paris exponent m_2 are slightly larger, which should be attributed to the conservative requirements for the standards and codes. Overall, all these values would fit in the 95% confidence bound obtained before.

On the other hand, the situation for the material constants in Stage I, i.e. C_1 and m_1, is far more complicated. According to the test result of Specimen 7, the proportion of cycles to reach a depth of 0.539 mm is about 36.65% of the entire life. The result of Specimen 10 shows the proportion of cycles to reach a depth of 0.451 mm is about 36.96% of the entire life. The difference in crack depth implies the uncertainty in this stage, even though these two specimens are quite comparable. It could be the result from the material heterogeneity in HAZ together with the behavior in the near-threshold region. However, it is not possible to draw a conclusion since only one or two data point are provided in Stage I. Even in BS 7910, the values of C_1 for the cases with different stress ratio are in various magnitude order.

As a result, it should be stated that the data in the present study is insufficient to predict the fatigue life that involves crack growth in Stage I, especially given the uncertainties in this stage. On this condition, it can be a practical way to assume that the initial cracks are
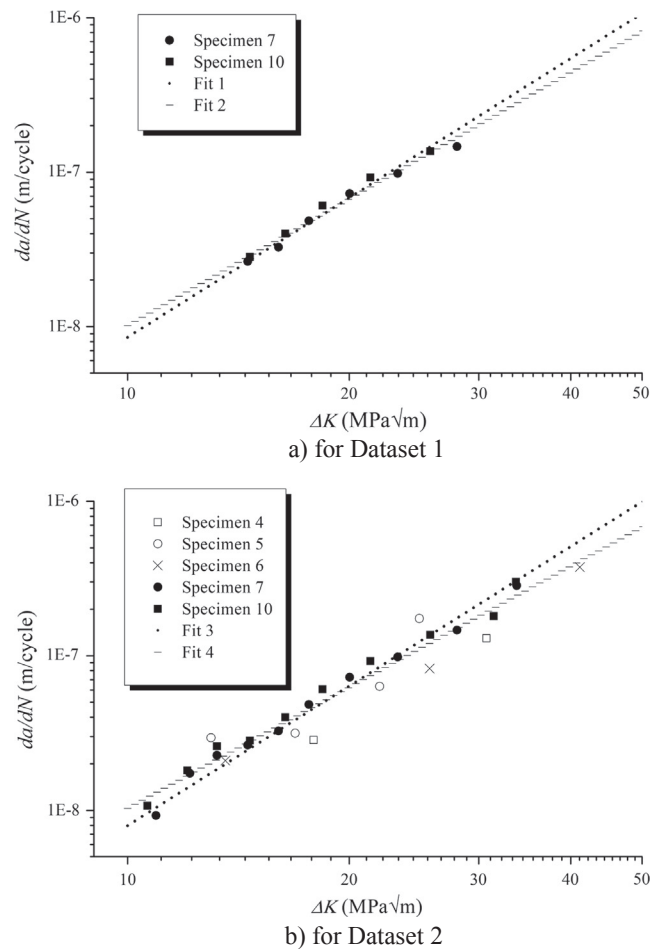

a) for Dataset 1

b) for Dataset 2

Fig. 21. Curve fitting to estimate the material constants.

actually smaller. The initial crack used here is an equivalent one based on the observations on the edge of the fracture face. Further investigation should be conducted using a different method to analyze its behavior in Stage I, since the production and precise identification of beach marks in this stage is next to impossible. Some discussions on this topic are also useful to give a more optimized definition of the initial crack on OSDs, while for which the crack growth behaviors in Stage I affected by the HAZ should be comprehensively investigated as well.

6. Conclusions

This paper presents a multiscale study on rib-to-deck welded joint of

Table 8

Comparison of material constants for different stages (da/dN in m/cycle and ΔK in MPa·m$^{0.5}$).

		Fit 2	IIW	Diff.	BS 7910 ($R < 0.5$)	Diff.	BS 7910 ($R \geq 0.5$)	Diff.
Stage I	C_1	\	\	\	7.59×10^{-17}	\	9.38×10^{-13}	\
	m_1	\	\	\	8.16	\	5.1	\
Stage II	C_2^{*}	1.91×10^{-11} (7.762×10^{-12}, 4.786×10^{-11})	1.65×10^{-11}	0.59%	1.41×10^{-11}	1.21%	2.70×10^{-11}	−1.42%
	m_2	2.73 (2.419, 3.033)	3	−9.00%	2.88	−5.21%	2.88	−5.21%
Transition point		\	\	\	9.96	\	4.5	\
ΔK_{th}		\	2	\	2	\	2	\

* The differences of Paris constant C_2 was calculated in logarithm coordinates.

OSDs with respect to the fatigue test, and establishes a method that enables to compute the SIFs in a numerical way. The conclusions can be drawn as follows.

Firstly, the crack growth process is traced using beach mark method in the test, and the fatigue behaviors including the crack initiation and growth are analyzed accordingly. It is found that the intergranular fracture in coarse-grained HAZ, which presents a different behavior on the fracture face, is the main reason for the crack initiation. By measuring it, the initial crack depth can be well indicated. Furthermore, the crack growth process shows that the fatigue cracks in the test are of small aspect ratio, a/c, as demonstrated by the long and shallow beach marks on the fracture face.

Secondly, the three-dimensional macroscopic model is built in SAMCEF with its XFEM module, but not fully applicable to the early-stage cracks due to computational ability limits. Hence, a two-dimensional local model is established using an XFEM program developed in MATLAB. It is linked to the macroscopic one in a non-concurrent way. The applicability and the accuracy are validated by comparing with previous studies and with the macroscopic model.

Afterwards, the SIFs for the whole crack growth process are obtained. As a result, different stages of crack growth are addressed, which are basically following the Paris law. However, part of Stage II seems to have fluctuations of CGRs, which could be the effect induced by the different materials in HAZ. Consequently, the material constant for fatigue crack growth, i.e. the Paris constant C, and the Paris exponent m, are achieved by curve fitting. By comparing with those given in standards and codes, the results are proved to be precise enough. It will benefit the fatigue assessment and the maintenance work for OSDs when combining with inspections. Nevertheless, due to the limited data points in Stage I and Stage II-a, future research is still needed as the majority of fatigue life will be spent on these stages.

Acknowledgments

References

[1] J.W. Fisher, Effect of Weldments on the Fatigue Strength of Steel Beams, Highway Research Board, National Research Council, 1970.
[2] R. Wolchuk, Lessons from weld cracks in orthotropic decks on three european bridges, J. Struct. Eng. 116 (1990) 75–84.
[3] F. De Jong, Overview fatigue phenomenon in orthotropic bridge decks in the Netherlands, 2004 Orthotropic Bridge Conference, Sacramento, (2004).
[4] Z.-G. Xiao, K. Yamada, S. Ya, X.-L. Zhao, Stress analyses and fatigue evaluation of rib-to-deck joints in steel orthotropic decks, Int. J. Fatigue 30 (2008) 1387–1397.
[5] H.-B. Sim, C.-M. Uang, Stress analyses and parametric study on full-scale fatigue tests of rib-to-deck welded joints in steel orthotropic decks, J. Bridge Eng. 17 (2012) 765–773.
[6] M. Yang, S. Kainuma, Y.-S. Jeong, Structural behavior of orthotropic steel decks with artificial cracks in longitudinal ribs, J. Construct. Steel Res. 141 (2018) 132–144.
[7] Q.-H. Zhang, C. Cui, Y.-Z. Bu, Y.-M. Liu, H.-W. Ye, Fatigue tests and fatigue assessment approaches for rib-to-diaphragm in steel orthotropic decks, J. Construct. Steel Res. 114 (2015) 110–118.
[8] Q.-H. Zhang, Y.-Z. Bu, Q. Li, Review on fatigue problems of orthotropic steel bridge deck, China J. Highway Transport. (2017) 14–30 + 39 (in Chinese).
[9] M.H. Kolstein, Fatigue Classification of Welded Joints in Orthotropic Steel Bridge Decks, Delft University of Technology, TU Delft, 2007.
[10] Z.X. Li, T.H.T. Chan, Y. Yu, Z.H. Sun, Concurrent multi-scale modeling of civil infrastructures for analyses on structural deterioration—Part I: Modeling methodology and strategy, Finite Elem. Anal. Des. 45 (2009) 782–794.
[11] Y. Sumi, T. Inoue, Multi-scale modeling of fatigue crack propagation applied to random sequence of clustered loading, Mar. Struct. 24 (2011) 117–131.
[12] M. Silani, S. Ziaei-Rad, H. Talebi, T. Rabczuk, A semi-concurrent multiscale approach for modeling damage in nanocomposites, Theoret. Appl. Fract. Mech. 74 (2014) 30–38.
[13] S. Hertelé, N. O'Dowd, K. Van Minnebruggen, M. Verstraete, W. De Waele, Fracture mechanics analysis of heterogeneous welds: validation of a weld homogenisation approach, Procedia Mater. Sci. 3 (2014) 1322–1329.
[14] B. Wang, H. De Backer, A. Chen, An XFEM based uncertainty study on crack growth in welded joints with defects, Theoret. Appl. Fract. Mech. 86 (Part B) (2016) 125–142.
[15] C.X. Li, X.S. Tang, G.B. Xiang, Fatigue crack growth of cable steel wires in a suspension bridge: multiscaling and mesoscopic fracture mechanics, Theoret. Appl. Fract. Mech. 53 (2010) 113–126.
[16] K.K. Tang, H. Wu, F. Berto, Fatigue data interpretation of 7075–T6 Al sheets by energy density factor in a dual scale model, Theoret. Appl. Fract. Mech. 79 (2015) 98–104.
[17] W. Nagy, B. Wang, B. Culek, P. Van Bogaert, H. De Backer, Development of a fatigue experiment for the stiffener-to-deck plate connection in Orthotropic Steel Decks, Int. J. Steel Struct. 17 (2017) 1353–1364.
[18] H.-B. Sim, C.-M. Uang, C. Sikorsky, Effects of fabrication procedures on fatigue resistance of welded joints in steel orthotropic decks, J. Bridge Eng. 14 (2009) 366–373.
[19] S. Kainuma, M. Yang, Y.-S. Jeong, S. Inokuchi, A. Kawabata, D. Uchida, Experiment on fatigue behavior of rib-to-deck weld root in orthotropic steel decks, J. Construct. Steel Res. 119 (2016) 113–122.
[20] S. Ya, K. Yamada, T. Ishikawa, Fatigue evaluation of rib-to-deck welded joints of orthotropic steel bridge deck, J. Bridge Eng. 16 (2011) 492–499.
[21] J. Neves, A. Loureiro, Fracture toughness of welds—effect of brittle zones and strength mismatch, J. Mater. Process. Technol. 153–154 (2004) 537–543.
[22] A. Hobbacher, Recommendations for Fatigue Design of Welded Joints and Components, second ed., Springer International Publishing, Switzerland, 2009.
[23] B. Wang, X.-Y. Zhou, H. De Backer, A. Chen, F. Schmidt, Macro-crack initiation life for orthotropic steel decks considering weld heterogeneity and random traffic loading, Struct. Infrastruct. Eng. 13 (2017) 1639–1652.
[24] K. Tanaka, Fatigue crack propagation from a crack inclined to the cyclic tensile axis, Eng. Fract. Mech. 6 (1974) 493–507.
[25] Y. Murakami, N. Hasebe, Stress Intensity Factors Handbook, Elsevier Science, 2001.
[26] J.C. Newman, I.S. Raju, An empirical stress-intensity factor equation for the surface crack, Eng. Fract. Mech. 15 (1981) 185–192.
[27] Y. Wang, Z.X. Li, A.Q. Li, Fatigue crack growth model for assessing reliability of box-girders for cable-stayed bridge combining SHMS with strain data, Theoret. Appl. Fract. Mech. 55 (2011) 60–67.
[28] BSI, BS 7910, Guide to Methods for Assessing the Acceptability of Flaws in Metallic Structures, British Standards Institution (BSI), London, 2013.